Adaptive mesh refinement method. Part 2: Application to tsunamis propagation

Kévin Pons, Mehmet Ersoy, Frederic Golay, Richard Marcer

Adaptive mesh refinement method. Part 2: Application to tsunamis propagation.

Kévin Pons, Mehmet Ersoy, Frédéric Golay and Richard Marcer

Abstract As an extension of "Adaptive mesh refinement method. Part 1: Automatic thresholding based on a distribution function.", we propose to show the efficiency of the automatic thresholding method for a large variety of real life test problems such as the propagation of tsunamis. The numerical simulations of multi dimensional large variety scale fluid-flows such as tsunami modeling, is still nowadays a challenging and a difficult problem. To this purpose, a parallel finite volume scheme on adaptive unstructured meshes for multi dimensional Saint-Venant system is presented. The adaptive mesh refinement method is based on a block-based decomposition (called BB-AMR) which allows quick meshing and easy parallelization. The main difficulty addressed here concerns the selection of the mesh refinement threshold which is certainly the most important parameter in the AMR method. Usually, the threshold is calibrated according to the test problem to balance the accuracy of the solution and the computational cost. To avoid "hand calibration", we propose to apply the automatic threshold method based on the decreasing rearrangement function of the mesh refinement criterion. The robustness was shown in the first part of this paper for the one dimensional Saint-Venant system. In this paper, this method

Kévin Pons
Principia S.A.S., Zone Athélia 1, 215 voie Ariane, 13705 La Ciotat cedex, France, e-mail: Kevin.Pons@principia.fr,
Université de Toulon, IMATH EA 2134, 83957 La Garde, France, e-mail: Kevin.Pons@univ-tln.fr

Mehmet Ersoy
Université de Toulon, IMATH EA 2134, 83957 La Garde, France, e-mail: Mehmet.Ersoy@univ-tln.fr

Frédéric Golay
Université de Toulon, IMATH EA 2134, 83957 La Garde, France, e-mail: Frederic.Golay@univ-tln.fr

Richard Marcer
Principia S.A.S., Zone Athélia 1, 215 voie Ariane, 13705 La Ciotat cedex, France, e-mail: Richard.Marcer@principia.fr

is applied to the two dimensional non homogeneous Saint-Venant system and successfully validated through several test cases comparing to experimental data.

1 Introduction

Many fluid flows problems arising in geophysics can be modeled with one or two dimensional depth-averaged equations. The Saint-Venant system is the simplest depth-averaged model [25, 38]. A number of related applications have been considered with depth-averaged approaches, such as sediment transport [14]; river flows, open channel, closed pipes, flooding [7, 8, 9, 10, 15, 16, 18]; atmosphere dynamics [20, 19]; landslides, debris flows, and avalanches [37, 23, 12, 22]; tsunamis propagation [33, 13] and the reference therein.

The most of fluid flows problems share the following features: the conservation laws include source terms, real flow can take place over a complex topography with eventually drying or flooding phenomena, non-trivial steady states and large variety of flows scales can appear. Therefore, the numerical simulation of such flows in complex multi dimensional configurations, especially for tsunamis propagation, is a challenging task. Adaptive mesh method allows, in principle, to solve in a reasonable CPU time accurately those scales. However, the efficiency of the AMR method depends on the accuracy of the mesh refinement criterion to indicate the region to refine or to coarsen and to the mesh refinement threshold. As discussed in the first part of this paper [41], in general, the threshold parameter is a tunable parameter which allows to balance between the accuracy of the numerical solution and the computational cost. The overall performance of the numerical scheme also depends on the data management within the parallel process. In order to spare proportionally the balanced distribution of CPU load, a Block-Based AMR method can be used (see for instance [28]).

In this paper, we present a multi dimensional finite volume numerical scheme to solve accurately and fast non-linear hyperbolic systems of conservation laws in the context of *parameterless* AMR framework. This scheme has been first presented by Ersoy et al. [17] for the one-dimensional gas dynamics equations for ideal gas, further extended to the dimension two and three and confronted to experimental data in [28, 1]. In these references, the numerical density of entropy production as a mesh refinement criterion have been used successfully using a tunable threshold parameter. The main objective of this paper is to improve the Block-Based AMR scheme [28] using the automatic mesh refinement method, proposed by Pons and Ersoy [41], for tsunamis propagation.

The paper is organized as follows. In Sect. 2, the tsunamis propagation problem is presented and the Saint-Venant equations are recalled and motivated within this context. Section 3 is devoted to the general presentation of the multi dimensional finite volume scheme. A particular attention is paid on the BB-AMR scheme using the automatic mesh refinement thresholding method. The model confrontation, and the numerical validation of the overall method, with experiments is presented

in Sect. 4. First, the numerical solution of the one dimensional numerical scheme is confronted to the flume experiments conducted at Oregon State University [44, 43]. These experiments involve the propagation, run-up and reflection of high amplitude solitary waves on a reef. Second, the numerical solution of the two dimensional scheme is confronted to the solitary wave propagation over a complex three dimensional shallow shelf [36]. In this experiment, the propagation, run-up, drying and flooding phenomena are involved. The last test concerns the Monai-Walley tsunami running-up onto a complex three dimensional beach [34]. All these test cases are useful to assert the efficiency of the automatic mesh refinement threshold method due to the involved waves propagations and multiple scales waves reflections.

2 Tsunamis propagation and the Saint-Venant equations

Tsunami is generally referred to any impulsed generated gravity wave. It can be generated by many sources. The most common tsunamis are a consequence of earthquake, landslide and volcanic explosion. Such events can displace a very large volume of water from its equilibrium. The displaced water mass, under the gravity action, attempts to come back to its equilibrium generating gravity waves. Depending of the tsunami source, the order of magnitude of a tsunami wave length is around several ten kilometers. Since this horizontal length is much larger than the oceans depth, vertically integrated model are generally used for tsunamis propagation. The most simple model is the Saint-Venant model for which the waves are non-dispersive. However, solving accurately this model over large scales still demand today high computational ressources [42]. Therefore it is essential to refine the mesh adaptively, especially close to the coast, in order to compute accurate solutions. Modeling the whole ocean with a fine resolution for all time is clearly unnecessary and even more for tsunamis propagation since its origin can be localized at some hundred of kilometers away. Therefore, the propagation of a tsunami can be efficiently simulated within the adaptive mesh refinement framework.

The Saint-Venant (or shallow water) equations are a non-linear hyperbolic system of partial differential equations for which whose solutions may contain shock waves. For this model, the characteristic propagation speed in any direction, is

$$c = \sqrt{gh(x,t)}$$

where $h(x,t)$ stands for the water elevation above the topography $Z(x)$ and $x \in \mathbb{R}^2$. These equations, being derived under the assumption of a hydrostatic pressure field, are well-known to be non-dispersive. It is also interesting to highlight that close to the shore, the shoaling phenomenon can be observed (i.e. whenever the wave starts to compress horizontally and grows vertically). For high shoaling effect, the non-linearities may become preponderant and the wave can break down. Because of the unique vertical evaluation, the solution of the Saint-Venant system cannot take into account such a solution. Nevertheless, a breaking wave can be represented

by a shock solution. More precisely, the speed of propagation and the amplitude of the breaking wave are rather well-represented through the shock wave ones, see for instance [6]. Therefore, the Saint-Venant model can be used to model several tsunami problems from the wave generation/propagation to the wave breaking.

The two dimensional non linear Saint-Venant system is

$$\begin{aligned} \partial_t h + \operatorname{div}(h\boldsymbol{u}) &= 0 \\ \partial_t (h\boldsymbol{u}) + \operatorname{div}(h\boldsymbol{u}^2) + \frac{g}{2}\nabla(h^2) &= -gh\nabla Z \end{aligned} \tag{1}$$

where the unknowns $h(x,t)$ and $\boldsymbol{u}(x,t) = (u_1, u_2)$ are respectively the height of the water and the depth-averaged velocity of the water at a space-time point (x,t), $x = (x_1, x_2) \in \mathbb{R}^2$ is the space coordinate, $t > 0$ is the time, g is the gravitational constant $g \approx 9.81\text{m/s}^2$ and $Z(x)$ is the topography term.

The three equations above express respectively, the conservation laws of mass and momentum in x_1 and x_2 direction driven by the flux

$$\boldsymbol{f}_1(\boldsymbol{w}) = \begin{pmatrix} hu_1 \\ hu_1^2 + \frac{g}{2}h^2 \\ hu_1u_2 \end{pmatrix} \text{ and } \boldsymbol{f}_2(\boldsymbol{w}) = \begin{pmatrix} hu_2 \\ hu_1u_2 \\ hu_2^2 + \frac{g}{2}h^2 \end{pmatrix}$$

and the source term

$$\boldsymbol{G}(x,\boldsymbol{w}) = \begin{pmatrix} 0 \\ -gh\partial_{x_1}Z \\ -gh\partial_{x_2}Z \end{pmatrix}$$

where the conservative variable $\boldsymbol{w}$ is

$$\boldsymbol{w}(x,t) = \begin{pmatrix} h \\ hu_1 \\ hu_2 \end{pmatrix} .$$

In its vectorial form, System (1) reads

$$\partial_t \boldsymbol{w} + \operatorname{div}\boldsymbol{f}(\boldsymbol{w}) = \boldsymbol{G}(x,\boldsymbol{w}) \tag{2}$$

where $\boldsymbol{f}(\boldsymbol{w}) = (\boldsymbol{f}_1(\boldsymbol{w}), \boldsymbol{f}_2(\boldsymbol{w}))$. We recall that the solutions of the above system can exhibit in finite time discontinuities, corresponding to hydraulic jumps or bores, even if the initial data $\boldsymbol{w}(x,0) = \boldsymbol{w}_0(x)$ is smooth.

System (2) can be also written in a quasi-conservation form as follows

$$\partial_t \mathbf{w} + \sum_{i=1}^{i=2} A_i \partial_{x_i} \mathbf{w} = \boldsymbol{G}(x,\mathbf{w}) \tag{3}$$

where A_i is the Jacobian matrix in the x_i direction

$$A_i = \frac{\partial \boldsymbol{f}_i}{\partial \boldsymbol{w}} . \tag{4}$$

From a numerical viewpoint, the two dimensional non conservative form (3) are less useful than in the one dimensional case since a simultaneous diagonalisation of A_1 and A_2 is not possible. Therefore the most of the schemes are based on a normal flux formulation as performed in this paper. In particular, in the case of Cartesian meshes, the flux formulation reduces to the one dimensional flux in the $(1,0)$ and $(0,1)$ directions. Therefore, without loss of generality, for any given control volume $\boldsymbol{V} \subset \mathbb{R}^2 \times [0,T]$ of outward unit normal vector $\mathbf{n} = (n_1, n_2)$, the Saint-Venant system (2) satisfies the following properties

Theorem 1.

1. *System* (2) *is strictly hyperbolic on the set* $\{h(x,t) > 0\}$ *where the eigenvalues are*

$$\lambda_1(h,\mathbf{u}) = \mathbf{u}\cdot\mathbf{n} - \sqrt{gh}, \qquad \lambda_2(h,\mathbf{u}) = \mathbf{u}\cdot\mathbf{n}, \qquad \lambda_3(h,\mathbf{u}) = \mathbf{u}\cdot\mathbf{n} + \sqrt{gh},$$

and the right eigenvectors are

$$\begin{aligned}
\mathbf{r}_1(h,\mathbf{u}) &= \left(1, u_1 - \sqrt{gh}n_1, u_2 - \sqrt{gh}n_2\right)^T, \\
\mathbf{r}_2(h,\mathbf{u}) &= \left(0, -\sqrt{gh}n_2, \sqrt{gh}n_1\right)^T, \\
\mathbf{r}_3(h,\mathbf{u}) &= \left(1, u_1 + \sqrt{gh}n_1, u_2 + \sqrt{gh}n_2\right)^T.
\end{aligned}$$

2. *For smooth solutions, the mean velocity u satisfies:*

$$\partial_t \mathbf{u} + \mathbf{u}\cdot\nabla\mathbf{u} + g\nabla(h+Z) = 0\,. \tag{5}$$

3. *For smooth solutions, the still water steady state, i.e. for* $\boldsymbol{u} = 0$*, reads*

$$gh + gZ = constant\,. \tag{6}$$

4. *System* (2) *admits a mathematical entropy :*

$$E(h,\mathbf{u},x) = \frac{h|\mathbf{u}|^2}{2} + \frac{gh^2}{2} + ghZ(x)$$

which satisfies the entropy (energy) relation

$$\partial_t E(h,\mathbf{u},x) + div\left(\left(E(h,\mathbf{u},x) + \frac{gh^2}{2}\right)\mathbf{u}\right) \leq 0 \tag{7}$$

where $|\mathbf{u}| := u_1^2 + u_2^2$.

Proof. Let $\boldsymbol{V} \subset \mathbb{R}^2 \times [0,T]$ of border ∂V and of outward unit normal vector $\mathbf{n}$. Then, let us integrate System (2) on $\boldsymbol{V}$ and apply the Green formula:

$$\partial_t \int_{\boldsymbol{V}} \mathbf{w}\, dx + \int_{\partial\boldsymbol{V}} \mathbf{f}(\mathbf{w})\cdot\mathbf{n}\, dv = \int_{\boldsymbol{V}} \boldsymbol{G}(x,\boldsymbol{W})\, dx\,. \tag{8}$$

The Jacobian matrix in the primitive variable of the flux across the normal $\mathbf{n}$ is then defined as

$$Jac = \left(\frac{\partial \boldsymbol{w}}{\partial \boldsymbol{W}}\right)^{-1} \frac{\partial \mathbf{f}\cdot\mathbf{n}}{\partial \mathbf{w}} \left(\frac{\partial \boldsymbol{w}}{\partial \boldsymbol{W}}\right)$$

where

$$\frac{\partial \mathbf{f}\cdot\mathbf{n}}{\partial \mathbf{w}} = \begin{pmatrix} 0 & n_1 & n_2 \\ (gh-u_1^2)n_1 - u_1u_2n_2 & 2u_1n_1+u_2n_2 & u_1n_2 \\ -u_1u_2n_1 + (gh-u_2^2)n_1 & u_2n_1 & u_1n_1+2u_2n_2 \end{pmatrix}$$

so that

$$Jac = \begin{pmatrix} 0 & n_1 & n_2 \\ (gh-u_1^2)n_1 - u_1u_2n_2 & 2u_1n_1+u_2n_2 & u_1n_2 \\ -u_1u_2n_1 + (gh-u_2^2)n_1 & u_2n_1 & u_1n_1+2u_2n_2 \end{pmatrix}$$

and the result immediately follows. The item 2. and 3. are obtained through a simple calculation.

For smooth solutions, the entropy equality (7) is obtained as the results of the addition of $h\times(5)\cdot\mathbf{u}+\left(\partial_t h+\operatorname{div}(h\boldsymbol{u})\right)\left(gh+gZ\right)$. Indeed, the first operation yields to

$$\begin{aligned} 0 &= h\Big(\partial_t \mathbf{u} + (\mathbf{u}\cdot\nabla)\mathbf{u} + \nabla\left(gh+gZ\right)\Big)\cdot\mathbf{u} \\ &= \partial_t\left(h\tfrac{|\mathbf{u}|^2}{2}\right) + \operatorname{div}\left(h\tfrac{|\mathbf{u}|^2}{2}\mathbf{u}\right) + h\mathbf{u}\cdot\nabla\left(gh+gZ\right) \end{aligned}$$

while the second one to

$$\begin{aligned} 0 &= \left(\partial_t h + \operatorname{div}(h\boldsymbol{u})\right)\left(gh+gZ\right) \\ &= \partial_t\left(g\tfrac{h^2}{2}+ghZ\right) + \operatorname{div}\Big(\left(gh^2+ghZ\right)\mathbf{u}\Big) - h\mathbf{u}\cdot\nabla\left(gh+gZ\right)\ . \end{aligned}$$

□

For weak solution Eq. (7) is an inequality. A numerical scheme preserving such inequalities for shallow water flows is stable. Moreover, the yielding inequality can be useful for adaptive mesh refinement as a mesh refinement criterion as performed in [17, 28, 1, 41] and the reference therein.

3 Finite volume approximation for the Saint-Venant system

This section summarizes the main features of the method, including the semi-discrete finite volume numerical approximation of a general non-linear hyperbolic system of equations (see Eqs. (2)) and the time integration. The mesh refinement procedure including the mesh refinement criterion and the automatic selection of the mesh refinement threshold are presented.

3.1 Multi dimensional finite volume approximation

The computational domain $\Omega \subset \mathbb{R}^d$ is split into a set of control volumes, also referred as cells, $\Omega = \cup_k C_k$ of mesh size $|C_k|$. The source term is upwinded at the cell interface through an hydrostatic reconstruction [3].

On a given cell C_k, noting $w_k(t)$

$$\boldsymbol{w}_k(t) \simeq \frac{1}{|C_k|} \int_{C_k} \boldsymbol{w}(t,x)\, d\boldsymbol{x}$$

the approximation of the mean value of the unknown $\boldsymbol{w}(t,x)$ on C_k at time t, and integrating (2) over each cell, we obtain:

$$\int_{C_k} \frac{\partial \boldsymbol{w}(t)}{\partial t} + \sum_a \int_{\partial C_{k/a}} \boldsymbol{f}(t,\boldsymbol{w}) \cdot \boldsymbol{n}_{k/a}\, ds = 0 \tag{9}$$

where $\boldsymbol{n}_{k/a}$ denotes the unit normal vector on the boundary $\partial C_{k/a}$ between cells k and a.

Next, $F\left(\boldsymbol{w}_k(t), \boldsymbol{w}_a(t), \boldsymbol{n}_{k/a}\right)$ the flux approximation being written

$$\boldsymbol{F}\left(\boldsymbol{w}_k(t), \boldsymbol{w}_a(t), \boldsymbol{n}_{k/a}\right) \approx \int_{\partial C_{k/a}} \boldsymbol{f}(t,\boldsymbol{w}) \cdot \boldsymbol{n}_{k/a} ds\ ,$$

the semi-discrete finite volume approximation of Eqs. (2) (see for instance [26, 45, 21]) is obtained:

$$\frac{\partial \boldsymbol{w}_k(t)}{\partial t} + \frac{1}{|C_k|} \sum_a \boldsymbol{F}\left(\boldsymbol{w}_k(t), \boldsymbol{w}_a(t), \boldsymbol{n}_{k/a}\right) = 0 \tag{10}$$

where $\boldsymbol{F}\left(\boldsymbol{w}_k(t), \boldsymbol{w}_a(t), \boldsymbol{n}_{k/a}\right)$ is defined via the Godunov solver, i.e. it is computed with the exact solution of the 1D Riemann problem at the interface k/a with the states $w_k(t)$ and $w_a(t)$ (for further details see, for instance, [45]).

Equations (2) are completed with the entropy inequality (7) where

$$(\nabla_w \boldsymbol{\psi}(s(\boldsymbol{w})))^t = (\nabla_w s(\boldsymbol{w}))^t\ D_{\boldsymbol{w}} f(\boldsymbol{w})\ .$$

The source term is upwinded at the cell interface following the hydrostatic reconstruction. It means that for each interface, the numerical flux

$$\boldsymbol{F}\left(\boldsymbol{w}_k(t), \boldsymbol{w}_a(t), \boldsymbol{n}_{k/a}\right)$$

is replaced by the flux at left hand side

$$\boldsymbol{F}_k\left(\boldsymbol{w}_k(t), \boldsymbol{w}_a(t), \boldsymbol{n}_{k/a}, \Delta Z_{k/a}\right)$$

and the right hand side $\boldsymbol{F}_a\left(\boldsymbol{w}_k(t), \boldsymbol{w}_a(t), \boldsymbol{n}_{k/a}, \Delta Z_{k/a}\right)$ of the interface k/a. These new fluxes are constructed as follows

$$\boldsymbol{F}_k\left(\boldsymbol{w}_k(t),\boldsymbol{w}_a(t),\boldsymbol{n}_{k/a},\Delta Z_{k/a}\right) = \boldsymbol{F}\left(\boldsymbol{w}_k^*,\boldsymbol{w}_a^*,\boldsymbol{n}_{k/a}\right) + \begin{pmatrix} 0 \\ \frac{g}{2}(h_k^2-(h_k^*)^2)n_1 \\ \frac{g}{2}(h_k^2-(h_k^*)^2)n_2 \end{pmatrix}$$
$$\boldsymbol{F}_a\left(\boldsymbol{w}_k(t),\boldsymbol{w}_a(t),\boldsymbol{n}_{k/a},\Delta Z_{k/a}\right) = \boldsymbol{F}\left(\boldsymbol{w}_k^*,\boldsymbol{w}_a^*,\boldsymbol{n}_{k/a}\right) + \begin{pmatrix} 0 \\ \frac{g}{2}(h_a^2-(h_a^*)^2)n_1 \\ \frac{g}{2}(h_a^2-(h_a^*)^2)n_2 \end{pmatrix}$$

by means of reconstructed states (i.e. satisfying still water steady state equation (6))

$$\begin{aligned}
\mathbf{w}_k^* &= (h_k^*,\mathbf{u}_k)\ , \\
\mathbf{w}_a^* &= (h_a^*,\mathbf{u}_a)\ , \\
h_k^* &= \max(0,h_k-\max(0,\Delta Z_{k/a}))\ , \\
h_a^* &= \max(0,h_a-\max(0,-\Delta Z_{k/a}))\ .
\end{aligned}$$

In theses formula, $\Delta Z_{k/a}$ stands for the jump of Z across the interface k/a. The scheme is therefore well-balanced by construction, i.e., the still water steady states are exactly satisfied.

Following Ersoy et al. [27, 17], the entropy inequality (7) is approximated using the semi-discrete finite volume scheme (10). The obtained discrete quantity, called the numerical density of entropy production, is then used as a mesh refinement criterion (see Sect. 3.3). For further details on the construction of the numerical scheme we refer to [17] since the definition of the numerical fluxes reduces to a one dimensional computational at each interface k/a. Up to now, the first and second order Godunov schemes are implemented.

3.2 Time integration

The time integration of Eqs. (10) and (7) can be achieved in a classical way either by a Runge-Kutta or Adams-Bashforth scheme. Note that, even if the Adams-Bashforth scheme is known to be less stable and less accurate, it can be easily handled in the framework of local time stepping to save computational time (see e.g. [2] or [17]). The local time stepping is not treated in this paper. The interested reader can found a detailed presentation in [17].

By integrating Eq. (10) (and (7)) during the time step $]t_n,t_{n+1}[$ of length δt_n and by evaluating the numerical fluxes at time t_n, the well-known first order Euler's scheme is obtained:

$$\boldsymbol{w}_k(t_{n+1}) = \boldsymbol{w}_k(t_n) - \frac{\delta t_n}{|C_k|}\sum_a \boldsymbol{F}\left(\boldsymbol{w}_k(t_n),\boldsymbol{w}_a(t_n),\boldsymbol{n}_{k/a}\right)\ . \tag{11}$$

In order to increase the accuracy, a second order Runge-Kutta method can be used as follows

$$\boldsymbol{w}_k(t_{n+1}) = \boldsymbol{w}_k(t_n) - \frac{\delta t_n}{|C_k|} \sum_a \boldsymbol{F}\left(\boldsymbol{w}_k(t_{n+1/2}), \boldsymbol{w}_a(t_{n+1/2}), \boldsymbol{n}_{k/a}\right)$$

where

$$\boldsymbol{w}_k(t_{n+1/2}) = \boldsymbol{w}_k(t_n) - \frac{\delta t_n}{2\,|C_k|} \sum_a \boldsymbol{F}\left(\boldsymbol{w}_k(t_n), \boldsymbol{w}_a(t_n), \boldsymbol{n}_{k/a}\right) \ .$$

The numerical density of entropy production (7) is then calculated with a second order Runge-Kutta scheme.

3.3 BB-AMR method

By contrast to the one dimensional case, defining a robust mesh refinement parameter for multi dimensional configurations is not enough to design a suitable numerical solver. The treatment of data is also a crucial point and in particular the way to share the memory in a parallel process. This point is handled in a hierarchical block-based way called BB-AMR. The global strategy to adapt the mesh and how to manage data are presented.

3.3.1 Mesh refinement method

The model framework and the related scientific issues have been detailed in recent above-mentioned publications. The overall principles of the Block-Based Adaptive Mesh Refinement (BB-AMR) scheme are briefly recalled in the case of a general non linear hyperbolic system

$$\begin{cases} \frac{\partial \boldsymbol{w}(t)}{\partial t} + \nabla \cdot \boldsymbol{f}(t, \boldsymbol{w}) = \boldsymbol{G}, & (t,x) \in \mathbb{R}^+ \times \mathbb{R}^d \\ \boldsymbol{w}(0,x) = \boldsymbol{w}_0(x), & x \in \mathbb{R}^d. \end{cases} \tag{12}$$

where $\boldsymbol{w}$, $\boldsymbol{f}$, $\boldsymbol{G}$ stand respectively for conservative variables, flux and source.

Mesh refinement criterion.

As a well-known result, the uniqueness of the (weak) solution is lost even if the initial data are smooth. It can be recovered by completing System (12) with an entropy inequality of the form:

$$S = \frac{\partial s(\boldsymbol{w})}{\partial t} + \nabla \cdot \boldsymbol{\psi}(\boldsymbol{w}) \leq 0 \ , \tag{13}$$

where (s, ψ) stands for a convex entropy-entropy flux pair. Even if we are not able to prove the uniqueness in the multi dimensional case, this inequality allows to select the physical relevant solution and provide a "smoothness" indicator since

the entropy satisfies a conservation equation only in regions where the solution is smooth and an inequality when the solution develops discontinuities. Thus, the discrete quantity S can always be considered as a measure of the amount of violation of the entropy equation (as pointed out in [5, 30, 32, 31, 17]). As already done in [17, 41], S, which is called the numerical density of entropy production, can be used as a smoothness indicator providing information on the need to locally refine the mesh (e.g. if the solution develops discontinuities) or to coarsen the mesh (e.g. if the solution is smooth and well-approximated). More precisely, Ersoy et al. [17] (see also [41]), have demonstrated that, for the one dimensional gas dynamics equation, the support of the relative error coincides with the support of the numerical density of entropy production. The extension toward the multi dimensional case is detailed in [28].

Automatic mesh refinement threshold.

However, as shown in Pons and Ersoy [41] (see also [40]), the numerical density of entropy production is a also a shock criterion indicator. Therefore, it may fails in the detection of smooth flows in the presence of shocks if the mesh refinement threshold is only based on the mean value of the criterion S_m. To overpass this drawback, following Pons and Ersoy [41], we use an automatic thresholding method based on the decreasing rearrangement (also known as distribution) function of the criterion. More precisely, this distribution function, for each threshold $\alpha \in (0, S_m]$, is the Lebesgue measure of the set $d(\alpha) = \{S(x) > \alpha\}$. It provides a complete description of the criterion and in particular local maxima are automatically sorted from the smallest to the largest. To define a "good candidate" for the threshold, we focus on the smaller local maxima corresponding to smooth flows. However, these maxima are hardly captured with the distribution function because it is numerically difficult to compute its derivatives. To overcome, Pons and Ersoy [41] propose to use the function $\alpha d(\alpha)$ for which the local maxima are easily computed numerically. The threshold is defined as follows

$$\alpha_{\mathrm{PE}} \text{ such that } \alpha_{\mathrm{PE}} d(\alpha_{\mathrm{PE}}) = \max_{0<\alpha\leqslant S_m} (\alpha d(\alpha)) \ .$$

In practice, the selected threshold is in general $\alpha_{\mathrm{PE}} < S_m$ for discontinuous flows and $\alpha_{\mathrm{PE}} \approx S_m$ for smooth flows. This nice feature allows in principle to balance the accuracy of the numerical solution and the computational cost. *Moreover, the adaptive process, in comparions with existing methods, is now parameterless.*

Numerically, we define the distribution function as follows. Let us consider a given discrete mesh refinement criterion $S(x,t_n) = \sum_{k=1}^{N} S_k^n \mathbb{1}_{C_k}(x)$ where N is the total number of cells at time t_n. Let $(\alpha_j)_{0\leqslant j\leqslant M}$ be an increasing sequence of $M+1$ threshold parameter such that $(\alpha_j)_{0\leqslant j\leqslant M} = \left(S_m \left(\frac{j}{M} \right)^2 \right)_{0\leqslant j\leqslant M}$. Then, the distribution function $d_j = d(\alpha_j)$ is

$$d_j = \#\{k \; ; \; S_k^n > \alpha_j\}$$

where # is the number of elements in the set $\{S_k^n > \alpha_j\}$.

Therefore, according to the finite volume approximation defined in Sect. 3, a local numerical entropy production S_k^n is computed on each cell at time t_n and compared to the mesh refinement threshold α_{PE}. Finally, for each cell C_k:

- if $S_k^n > \alpha_{\mathrm{PE}}$, the mesh is refined and,
- if $S_k^n < \alpha_{\mathrm{PE}}$ the mesh is coarsened.

3.3.2 BB-AMR process

For the one dimensional case, the local mesh refinement procedure is constructed following dyadic tree applied at each time step. “Macro cells” are used to be easily refined by generating hierarchical grids. Each cell can be split in two. Dyadic cells graph are thus produced, in basis 2 numbering, to allow a quick computing scan to determine the adjacent cells. For stability reasons, the mesh refinement level cannot exceed 2 between two adjacent cells. More details can be found in [17].

The multi dimensional extension of the mesh refinement procedure is a difficult task. Interesting works have been presented for 2D Cartesian grid or quad-tree [4, 47, 39, 48], octree for 3D simulations [35, 24], and anisotropic AMR [11, 29]. For the Saint-Venant system (1) the extension from 1D to 2D leads naturally to quad-tree meshing. But, the presence of a complex moving interface (composed of rarefaction and shocks) implies to re-mesh at each time step, which is obviously a costly process. Guided by the need to reach a relevant compromise between the contradictory aims of solution accuracy and computing speed, a Cartesian block-based mesh approach is introduced, somehow like in [46, 49]. If the mesh is not refine at each time step, the patch where the grid should be refine must be enlarged. The grid generation in the framework of BB-AMR can be developed as follow.

- Firstly, the initial computational domain is divided in several hexahedral elements, called blocks. For the sake of simplicity, Fig. 1(a) represents a regular quadrilateral mesh.
- Secondly, we define for each block a discretization n_x in x-direction, n_y in y-direction and a level of refinement l_r such that the total number of cell in x-direction of the block will be $2^{l_r} n_x$. As the mesh refinement level cannot exceed 2 between two adjacent blocks, the level of mesh refinement is automatically adapted if necessary (as for example for the blocks $B5$ and $B2$ in Fig. 1(b))
- Thirdly, in order to balance the CPUs load, the cells of each block are redistributed in a fixed number of domains according to the Cuthill-McKee numbering, see Fig. 1(c).
- Finally, the unstructured mesh is built for each domain (see Fig. 1(d)).

For each refined cells (or blocks), averaged values are projected on each sub-cell and fluxes are computed as simply as possible to avoid heavy computation. At the

interface between two domains, ghost cells are created in order to transfer the necessary data to the explicit time integration scheme at each time step.The number of domain being fixed, each domain are loaded in a given MPI process. These MPI processes are then load on a fixed number of cores (not necessary the same).

The re-numbering and re-meshing being expensive, the mesh is finally kept constant on a time interval, called AMR time-step, given by the smallest block (rather by the smallest cell) and the maximum velocity. Details on the BB-AMR are given in [28, 1].

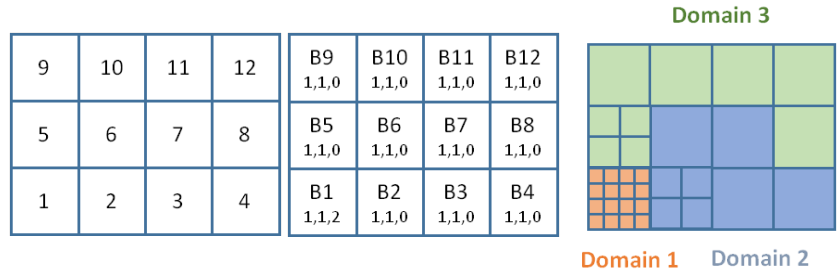

(a) Initial grid domain 0 (b) Block B_i (n_x, n_y, l_r) (c) Refined mesh and domains

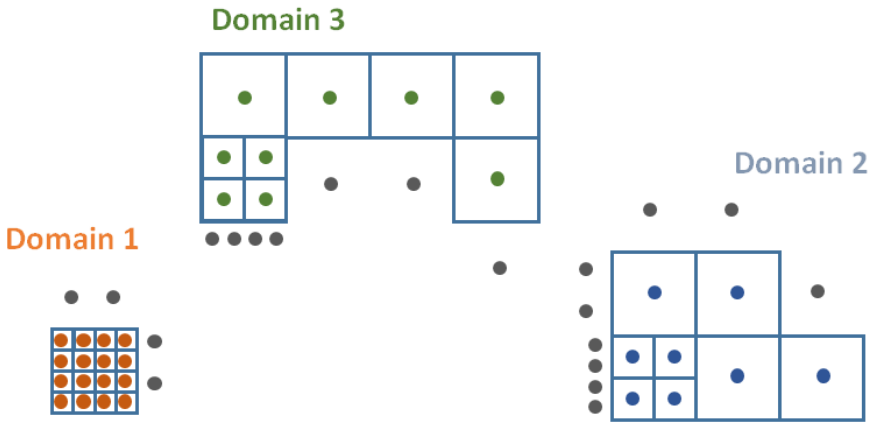

(d) Mesh generation

Fig. 1 BB-AMR process

4 Real-life Applications

As a natural extension of the work [41] and [28, 1], we show the overall performance of the BB-AMR scheme with automatic thresholding confronted to experimental and state-of-the-art numerical results[1].

For each test case, the numerical simulations are carried out on adaptive grids (using the BB-AMR method previously presented) and on uniform grids. The comparisons of both simulations allow to show the reliability and the efficiency of the parameterless adaptive method.

4.1 Solitary wave propagation over a two dimensional reef

This benchmark aims at reproducing a set of laboratory experiments carried out at the O.H. Hinsdale Wave Research Laboratory, Oregon State University (OSU, see Roeber *et al.* [44] and Roeber and Cheung [43]). These experiments involve the propagation, run-up, splash-up and reflection of high amplitude solitary waves on two-dimensional reefs. Their purpose is on one hand to investigate processes related to breaking, bore formation, dispersion, and passage from sub- to super-critical flows, and on the other hand, to provide data for the validation of near-shore wave models in fringing reef. Even if the Saint-Venant model (2) is not relevant for dispersive flows, through this test case we show that globally experimental data are well-captured and the threshold parameter is automatically well-chosen.

4.1.1 Experimental settings.

The geometry of the test considered here is shown in Fig. 2. The length of the basin is of 104 m, however the computational domain is delimited by a reflecting wall placed at $x = 83.7$ m. The reef starts at $x = 25.9$ m with a nominal slope of $1/12$. The actual slope is such that the height of 2.36 m is reached after $x = 28.25$ m. At this station a 0.2 m height crest is mounted. The offshore slope of the crest is the same of the reef, and the length of its plateau is of 1.25 m. The on-shore side has a slope of $1/15$ giving a nominal length for the crest basis of 6.65 m (using the actual offshore slope, a crest basis of 6.644 m is obtained). For the computations, the use of the nominal slope values is prescribed. This gives an offshore length of the crest slope (starting at 28.25 m) of 2.4 m. Therefore, with the notations used in this paper, the bathymetry is

[1] The numerical soft used for the following test cases is the EOLENS code developed by IMATH (Institut de Mathématiques de Toulon) and Principia.

$$Z(x) = \begin{cases} -2.5 & \text{if } x < 25.9\,, \\ \frac{(x-25.9)}{30.8} 2.565 - 2.5 & \text{if } 25.9 < x < 56.7\,, \\ 0.065 & \text{if } 56.7 < x < 57.65\,, \\ \frac{(57.95-x)}{3} 0.2 + 0.0650 & \text{if } < 56.7 < x < 60.95\,, \\ -0.1360 & \text{if } x > 60.95\,. \end{cases}$$

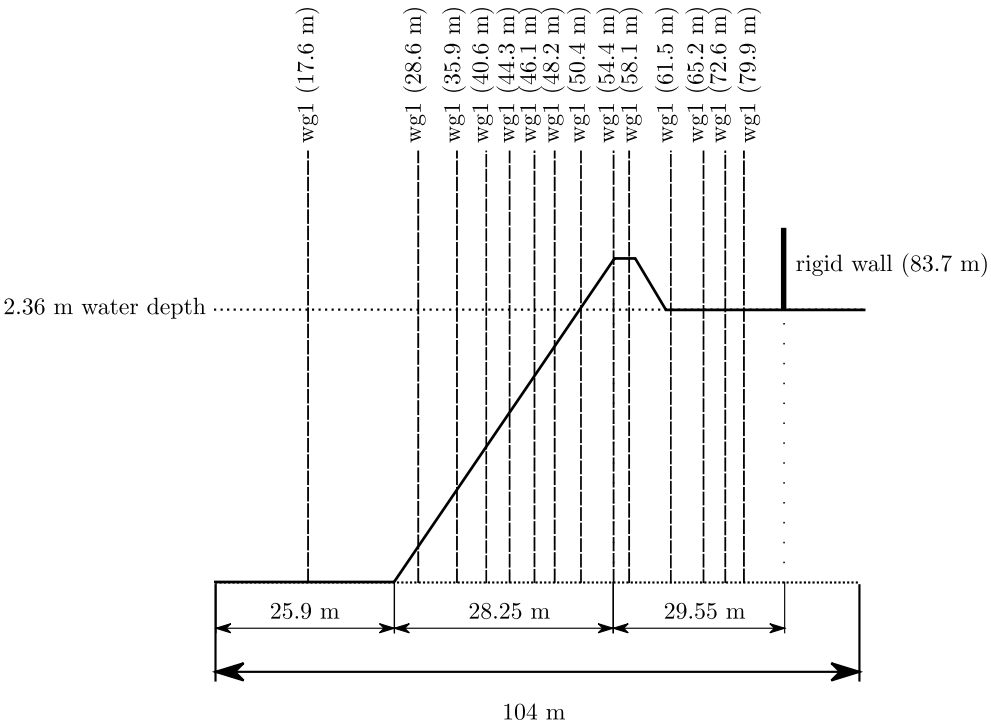

Fig. 2 Experimental settings and wave gauges locations

The initial depth at still water is $h_0 = 2.5$ m, yielding to a partially submerged crest, and a depth behind it (on-shore side) of 0.14 m. The initial solution consists of a solitary wave of amplitude $A = 0.75$ m providing a non linearity ratio of $\frac{A}{h_0} = 0.3$. For numerical purpose, the initial data consist of a solitary wave centered at $x_0 =$ 17.6 m of amplitude

$$\eta(x,0) = \frac{A}{\cosh\left(\sqrt{\frac{3A}{(4h_0^3)}}(x-x_0)\right)^2} \tag{14}$$

and velocity

$$u(x,0) = \sqrt{g(h_0+A)}\eta(0,x)/h_0 \tag{15}$$

which corresponds to the experimental data at the dimensionless time $\tilde{t} = t\sqrt{\frac{g}{h_0}} = 55.03$ as displayed in Fig. 3(a). In these expressions η is $\eta = h + Z$.

4.1.2 Experimental results.

Figures 3(a) and 3(b) shows the propagation of the solitary wave over the slope starting at $x = 25.9$. Figure 3(c) represents the surface elevation at the dimensionless time $\tilde{t} \approx 69$ s where the wave develops into a plunging breaker onto the reef crest[2]. From an experimental viewpoint, $\tilde{t} \approx 69$ s corresponds to the subsequent time of overturning of the free surface. In Fig. 3(d), the wave hitting the free surface creates a downstream and upstream propagating bore as shown in Fig. 3(e). The downstream propagating bore is reflected at the end wall at $x = 83.7$ m and propagates in opposite direction as displayed in Fig. 3(f).

4.1.3 Numerical results

In Figs. 3(a)–3(f), the experimental surface elevation (represented with blue circles) over the bathymetry Z for several dimensionless time $\tilde{t}$ are compared to the obtained numerical results (green and red lines-circles) [3]. The numerical solution is computed on a uniform grid composed of 1000 cells and on an adaptive grid initially composed of 200 cells with $l_{\max} = 4$ where $l_{\max}$ is the maximum level of the mesh refinement. For both numerical experiments, the CFL number is set to 0.99. Free boundary condition at $x = 0$ and reflecting boundary condition at $x = 83.7$ are imposed. Table 1 summarizes the numerical parameters used for this test case.

	Adaptive mesh simulation	Uniform mesh simulation
Simulation time	240	240
Number of cells	200-560	1000
Remeshing time step	0.05 s	not applicable
Time order integration	1	1
Space order integration	1	1
CFL	0.99	0.99
Boundary conditions	reflectives	reflectives

Table 1 Numerical parameters

[2] The authors would thanks V. Roeber to furnish the experimental data of this test case

[3] Intel(R) Core(TM) i5-2500 CPU @ 3.30GHz

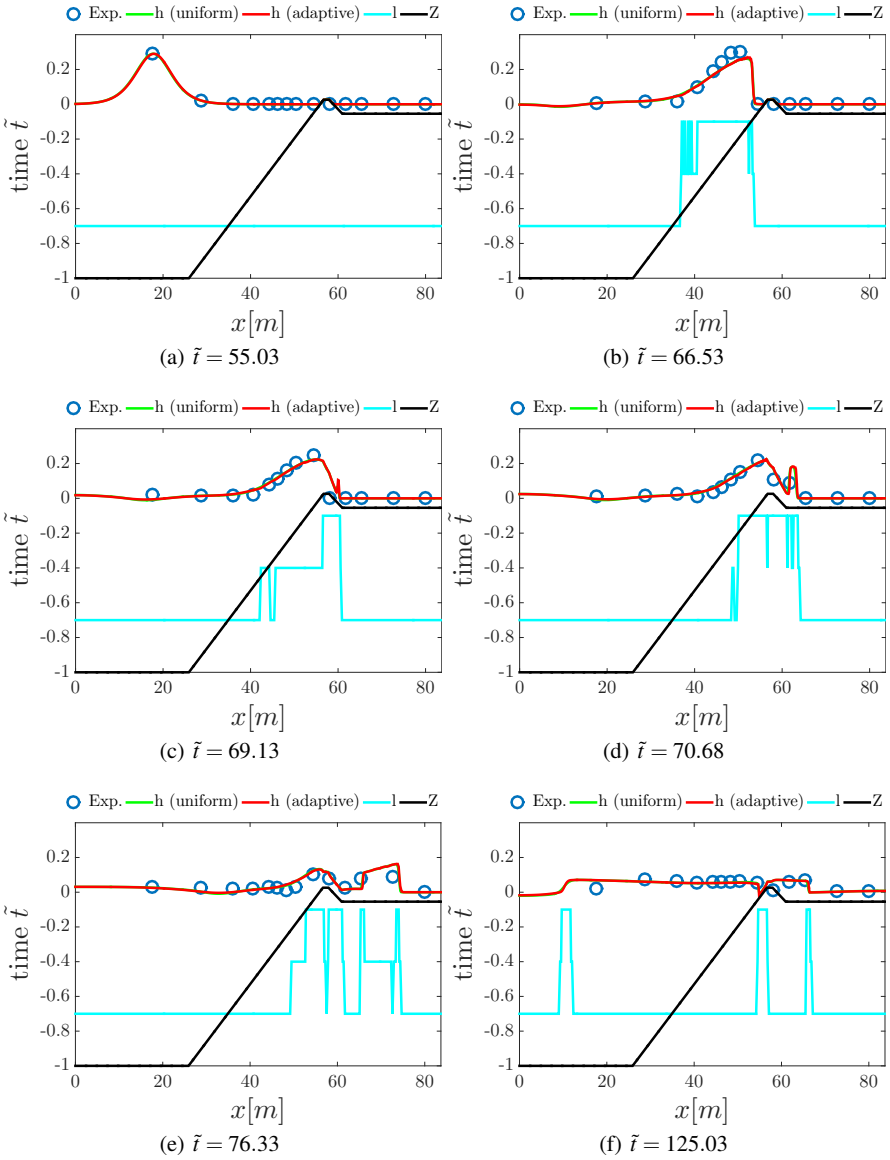

(a) $\tilde{t} = 55.03$ (b) $\tilde{t} = 66.53$

(c) $\tilde{t} = 69.13$ (d) $\tilde{t} = 70.68$

(e) $\tilde{t} = 76.33$ (f) $\tilde{t} = 125.03$

Fig. 3 Surface profiles of solitary wave propagation over an exposed reef crest. Confrontation of experimental data (blue circles) to numerical data computed on a uniform grid (solid green line) and on an adaptive grid (solid red lines). The solid cyan line represents the mesh level and the black one the bathymetry

4.1.4 Numerical vs experimental results.

The obtained numerical results as shown in Figs. 3(a)–3(f) are rather well-computed when compared to experimental data. However, the wave height is slightly underestimated (see Fig. 3(c)) while the hydraulic bore propagation front height is overestimated (see Fig. 3(d)).

We now compare in Figs. 4(a)–4(f), the computed and the experimental water elevation at the wave gauges displayed in Fig. 2. The oscillating shape of the experimental measures almost corresponds to dispersive effects which cannot be detected with the Saint-Venant model (2). However, the shape of the numerical results almost coincides with the experimental data for wave gauges located before $x = 54.4$ m as shown in Figs. 4(a)–4(c). The point $x = 54.4$ m is located just before the crest and in particular it corresponds to the region where the overturning of the free surface is experimentally observed. It yields numerically to a small shift as observed in Figs. 4(d)–4(f).

4.1.5 Numerical results: adaptive vs uniform grid computation.

The adaptive scheme uses an average of 356 cells against 1000 cells (see Fig. 5(b)) for the uniform one and the CPU-time is 95 s against 210 s.

We observe that the computation on adaptive grid is comparable to the numerical solution on uniform grid and computed about 2 times faster with less cells. We see also in Figs. 3(a)-3(f) that for each time step, the threshold parameter is automatically well-set to capture efficiently the region to refine (see also Fig. 5(a)). During the first 50 non-dimensional time, we have already pointed out that the solitary wave propagates and splash-up. This phenomenon is characterized by a discontinuous or sharp gradient flow for the Saint-Venant system, see Fig 3. In view of the remarks in Sect. 3.3.1, we observe that for almost all $\tilde{t} \in (55, 100)$, the threshold is set to $\alpha_{\mathrm{PE}} < S_m$. For $\tilde{t} > 100$, the flow is almost smooth and therefore $\alpha_{\mathrm{PE}} \approx S_m$. Therefore, we recover the behavior predicted in Pons and Ersoy [41] and in view of the confrontation with the computation on uniform grid, this test shows the reliability/efficiency of the automatic selection of the threshold for multiple scale flows.

4.2 Solitary wave propagation over an irregular three-dimensional shallow shelf

In this test case, the numerical simulation of a solitary wave propagation over a complex three dimensional bathymetry is performed. This test case was experimentally introduced in [36] to understand the turbulence and kinematic properties associated with a breaking solitary wave.

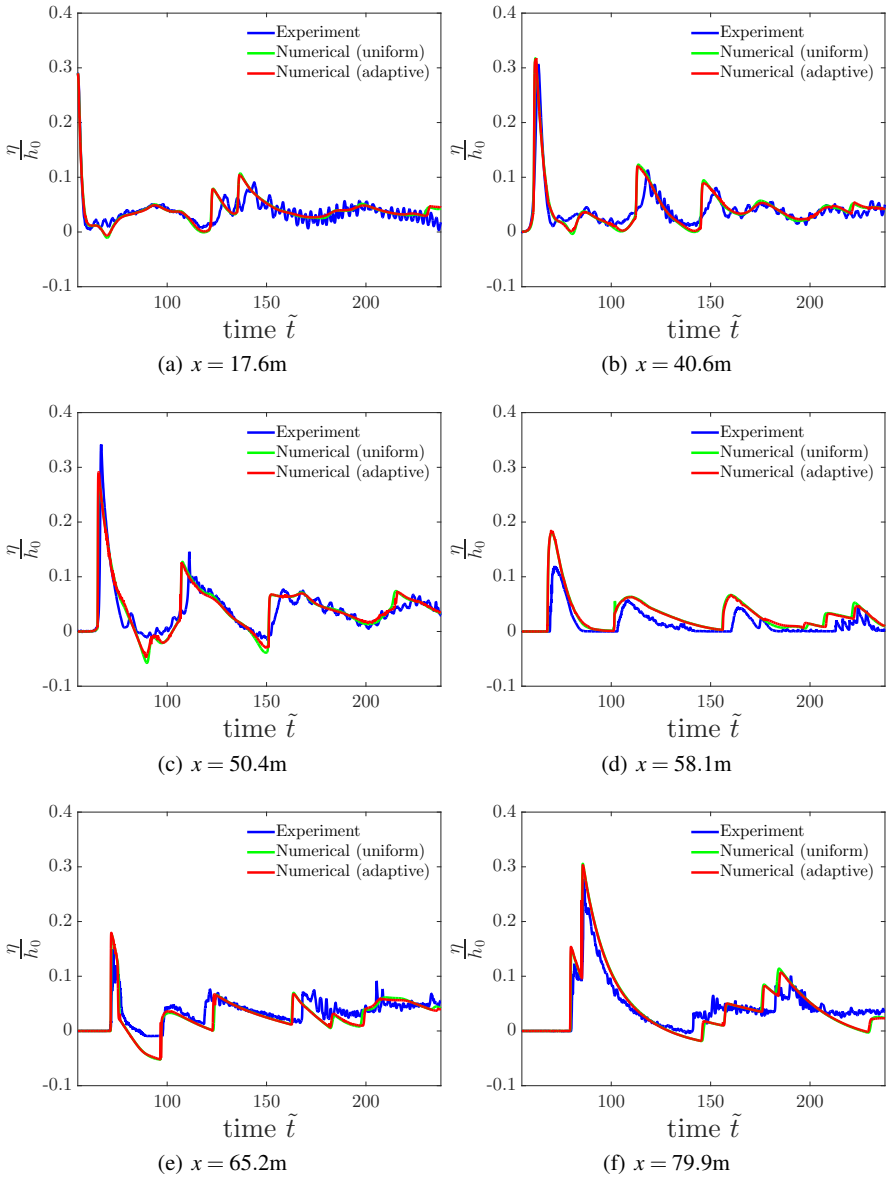

(a) $x = 17.6$m (b) $x = 40.6$m

(c) $x = 50.4$m (d) $x = 58.1$m

(e) $x = 65.2$m (f) $x = 79.9$m

Fig. 4 Surface profiles of solitary wave propagation in time at wave gauges 1 to 6. Confrontation of experimental data (solid blue line) to numerical data computed on a uniform grid (solid green line) and on an adaptive grid (solid red line)

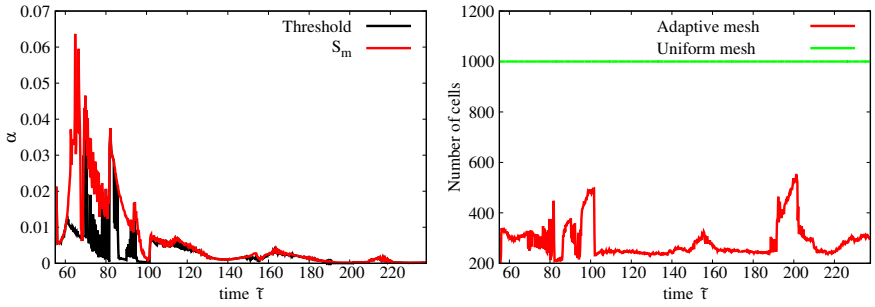

(a) Threshold (b) Number of cells

Fig. 5 Time evolution of the mesh refinement threshold and the number of cells

4.2.1 Experimental settings.

A laboratory experiment was conducted in a large wave basin which was 48.8 m long and 26.5 m wide at Oregon State University for which free surface elevations and fluid velocities were recorded at several locations by wave gauges (WG) and velocity captors (ADV). A single solitary wave of height of 39 cm at $x = 5$ is produced with a piston-type wave-maker over a complex bathymetry illustrated in Fig. 6. The bathymetry begins with a flat part allowing to generate properly a solitary wave. Then, starting at 10.2 m of the wave-maker and extending to $x = 25.5m$, a complex three dimensional shelf was built. The associated slope to this zone is variable but less and less steep. After that, a very small one dimensional slope finishing on a flat onshore zone was built. The experimental basin is closed by walls. For further informations on this experiment, interested readers can found more details in [36]. The domain is numerically extended to $x = -5$ m with a water depth of 78 cm to impose a solitary wave instead of reproducing the wave maker movement. The simulated solitary wave is a first order solution of the Boussinesq equation (see Eqs. (14) and (15)) with $x_0 = 5m$ and $\frac{A}{h_0} = 0.5$. Fluid height and velocities are recorded during 45 s. Finally, the material used for the walls and the bathymetry were made of smooth concrete so that one can assume almost a frictionless flow.

4.2.2 Numerical results.

For numerical purpose, we have considered 128 initial blocks composed of 7 500 cells for the initialization of the adaptive computation and almost 33 000 cells for uniform mesh computation. For both simulations, the CFL number is set to 0.5. Reflecting boundary conditions are prescribed to walls. Table 2 summarizes the numerical parameters used for this test case.

In Fig. 7, the adaptive numerical solutions calculated at time $t = 0.5$ s (see Fig. 7(a)), $t = 2.5$ s (see Fig. 7(b)), $t = 5.75$ s (see Fig. 7(c)) and $t = 23.75$ s (see Fig.

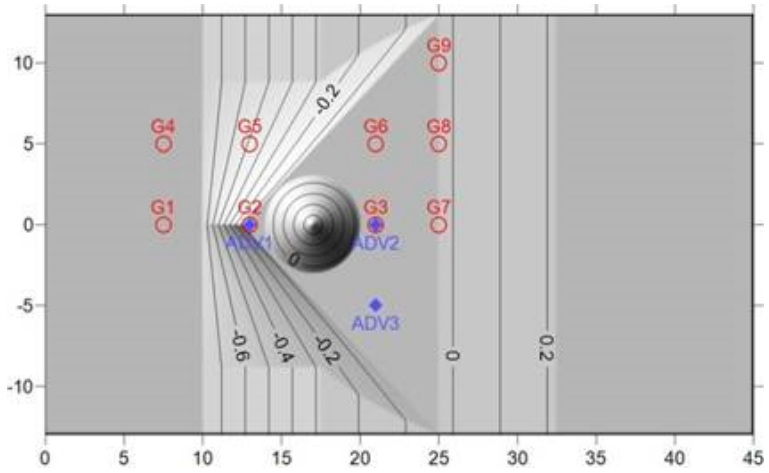

Fig. 6 Experimental settings

	Adaptive mesh simulation	Uniform mesh simulation
Simulation time	30 s	30 s
Number of blocks	128	128
Number of cells	7 500-25 000	33 000
Remeshing time step	0.25 s	not applicable
Time order integration	2	2
Space order integration	2	2
CFL	0.5	0.5
Boundary conditions	reflectives	reflectives

Table 2 Numerical parameters

7(d)) are represented. The Fig. 7(a) represents the profile of the solitary wave which propagates towards the coast. Figures 7(b) and 7(c) show respectively the wave hitting the conic island and then the beginning of the flooding. Figure 7(d) shows the flow after the wave run-up and its reflection on the right side of the wall.

To highlight the efficiency of the mesh refinement parameter and the automatic selection of the threshold, the numerical density of entropy production (without absolute value) is displayed at several times in Fig. 8, (time $t = 0.5$ s in Fig. 8(a), for $t = 2.5$ s in Fig. 8(b), for $t = 5.75$ s in Fig. 8(c) and for $t = 23.75$ s in Fig. 8(d)). It can be noticed that according to the flow, first the numerical density of entropy production indicates which areas need to be refined and second, the mesh refinement threshold is well chosen with the method described in Sect. 3.3.1, see also [41] for further details. For instance, in Fig. 7(c), the region which needs to be refined is clearly the zone around the ”conic island”. According to Fig. 8(c), the numerical density of entropy production in this area shows that the local maxima (lowest value without the absolute value) are of almost of order 0.005 and clearly

follows the wave front. We see in Fig. 11(a), approximately at time $t = 5.75$ s, that the threshold is automatically fixed to almost 0.001 and therefore allows to perform a suitable refinement in the region of interests as observed in Fig. 7(c) or 8(c).

4.2.3 Numerical vs experimental results.

Next, the numerical results are confronted to the experimental data recorded at the waves gauges 2, 4, 6 and 7 (WG) for the water height, see Fig. 9, and to the velocity captors 2 and 3 (ADV) for the first u component of the velocity vector, see Fig. 10.

For the wave gauge 2 to 7 (see Figs. 9(a)–9(d)), the global shape of the free surface is in quite good agreement with the experimental data but some differences are observed. The numerical solution computed with the Saint-Venant system (2) slightly underestimates the water level at the wave gauge 2 (see Fig. 9(a)) and overestimates at the wave gauge 4 (see Fig. 9(b)). Moreover, the numerical solution is rather accurate up to time $t = 15$ s at the wave gauges 6 and 7 (see Fig. 9(c) and 9(d)). For $t \geqslant 15$ s, the dispersive effects, not reproduced with the Saint-Venant system, begin significant and show slightly different results between experimental and numerical data. Similar conclusion can be drawn up for the first component of the vector velocity on the captor 2 (see Fig. 10(a)) and 3 (see Fig. 10(b)).

4.2.4 Numerical results: adaptive vs uniform grid computation.

Compared to the computation on a uniform grid (see Figs. 9 and 10), the adaptive mesh refinement scheme requires only an average of 13000 cells against 33000 cells. For the same accuracy, the adaptive scheme allows to save almost 60% of cells with respect to the uniform mesh. During the adaptive simulation, the maximum refined area is reached around the time $t = 12$ s which corresponds to the time where the free surface oscillates behind the island and the wave run-up on the "coast". All these cells saved allow to speed up the computation by 2.5 time for this test case. Let us also emphasize that, as done in [17], an implementation of a local time stepping method can also decrease the global CPU-time. Moreover, one can see in Fig. 11(a) and 11(b), the time evolution of the mesh refinement threshold and the number of cells during the numerical experiment.

4.3 Tsunami runup onto a complex three dimensional Monai-Walley beach

This test case concerns the Hokkaido-Nansei-Oki tsunami, in 1993, that struck the Okushiri Island in Japan. The tsunami run-up records was about 30 m height and the

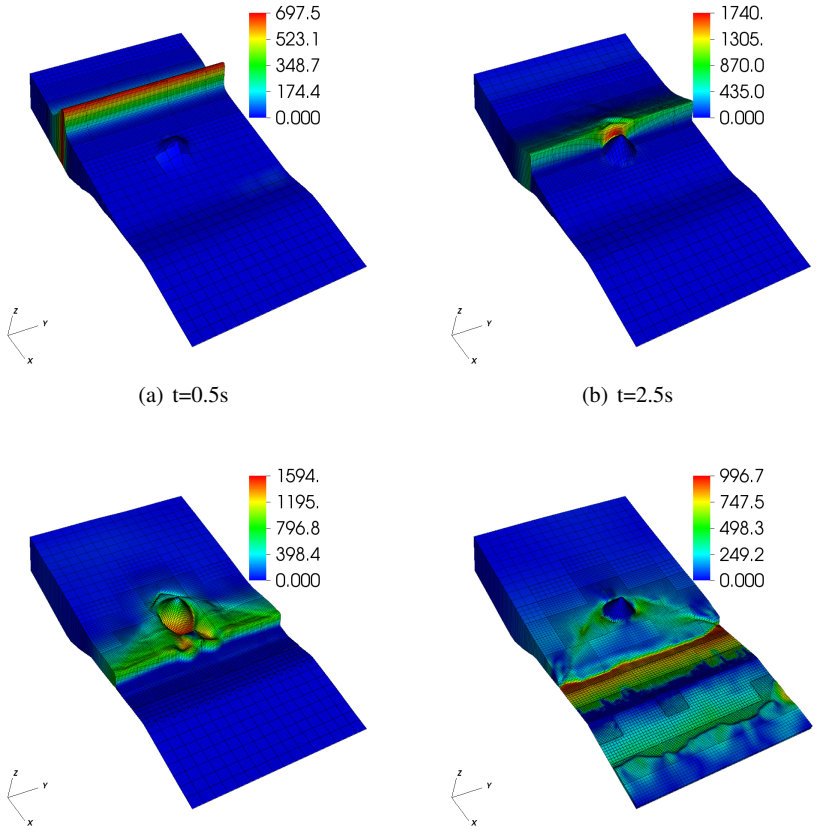

(a) t=0.5s (b) t=2.5s

(c) t=5.75s (d) t=23.75s

Fig. 7 Numerical water height (coloration is issue from the kinetic energy)

currents speed of order 10-18 m/s for which relevant high-quality data were saved [4]. The largest value run-up (32 m) was recorded near the Monai-Walley beach.

4.3.1 Experimental settings.

To understand the complex run-up, a 1/400 scale laboratory model of Monai was realized in a large-scale tank of 205 m long, 6 m deep, and 3.5 m wide at the Central Research Institute for Electric Power Industry (CRIEPI) in Abiko (Japan). The off-

[4] Several sources and data can be found, see for instance `http://nctr.pmel.noaa.gov/benchmark/Laboratory/Laboratory\_MonaiValley/` or `http://isec.nacse.org/workshop/2004_cornell/bmark2.html`

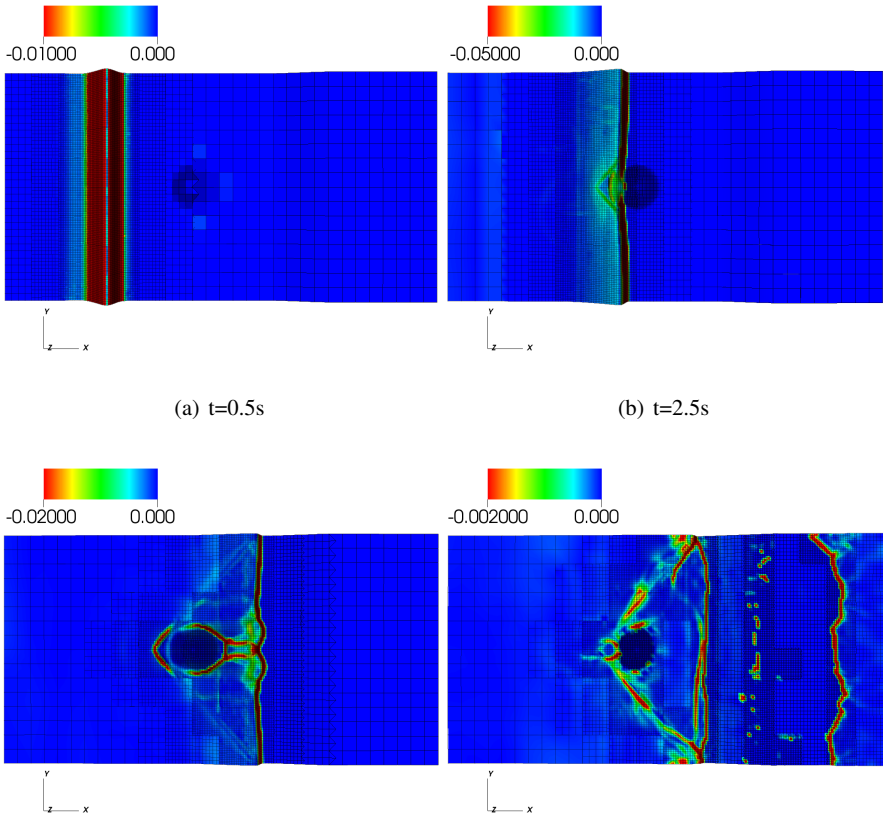

(a) t=0.5s (b) t=2.5s

(c) t=5.75s (d) t=23.75s

Fig. 8 Adaptive mesh (coloration is issue from the numerical density of entropy production without absolute value)

shore incident wave on a water depth d = 13.5 cm is prescribed. There are reflective vertical side-walls at $y = 0$ and 3.5 m as for the x boundaries. The bathymetry as well as the coastal topography reproduced in the laboratory experiment are represented[5] in Fig. 12(b) and 12(c) .

The input wave at $x = 0$ m is a leading-depression height of -2.5 mm with a crest of 1.6 cm behind it, as displayed in Fig. 12(a). In the experiment, the waves are measured at thirteen locations and complete time histories are given at three locations, (x, y) = (4.521, 1.196), (4.521, 1.696), and (4.521, 2.196) in meters, see also [34].

[5] sources and pictures are available at `http://isec.nacse.org/workshop/2004\_cornell/bmark2.html`

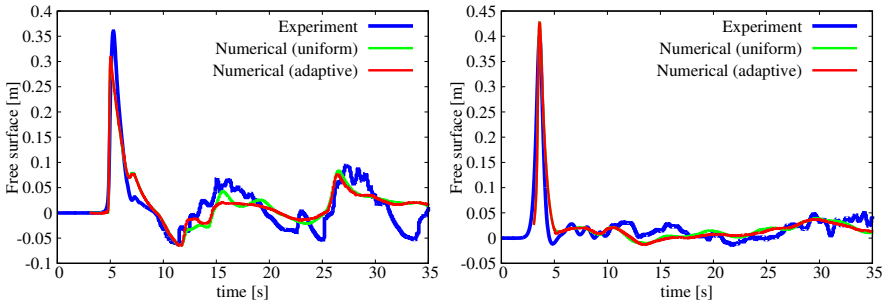

(a) WG2 results (b) WG4 results

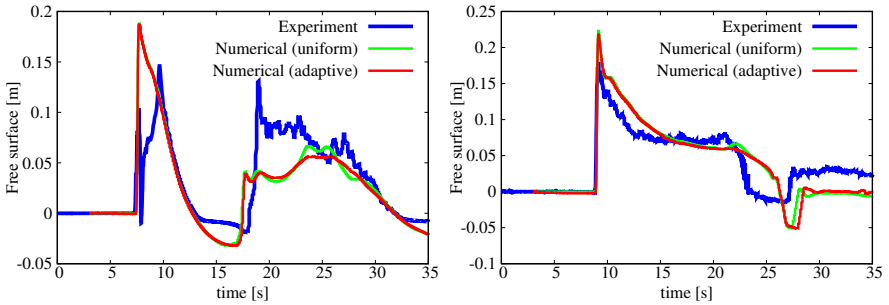

(c) WG6 results (d) WG7 results

Fig. 9 Free surface results at different positions : experimental data versus numerical simulation with and without mesh adaptivity

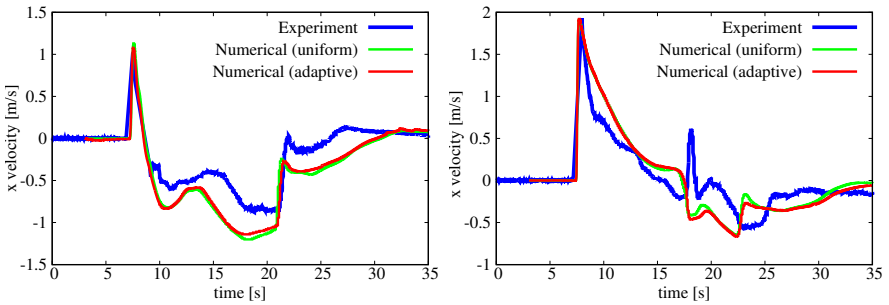

(a) ADV2 u results (b) ADV3 u results

Fig. 10 Velocity results at different positions : experimental data versus numerical simulation with and without mesh adaptivity

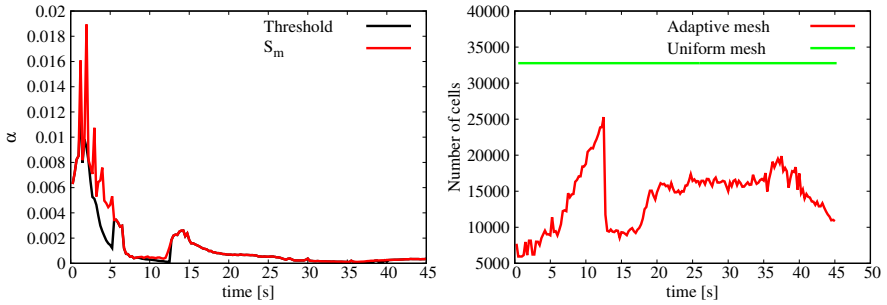

(a) Threshold (b) Number of cells

Fig. 11 Time evolution of the mesh refinement threshold and the number of cells

In contrast with the previous experimental test cases, the dispersive phenomena can be neglected here.

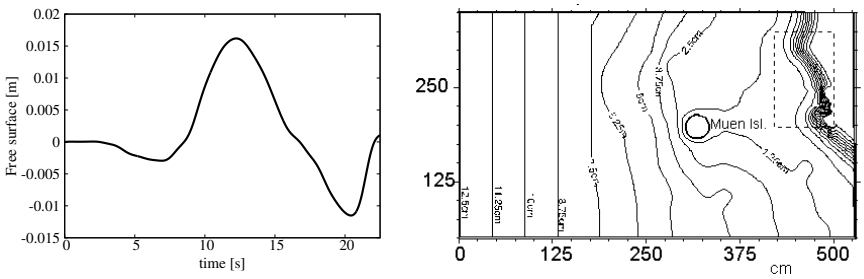

(a) Initial wave profile (b) Top view

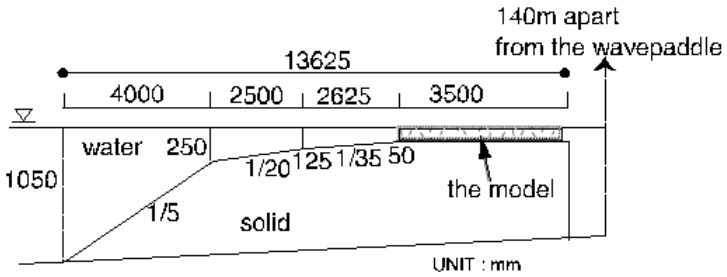

(c) Side view

Fig. 12 Experimental settings

4.3.2 Numerical results.

The initial condition for this experimental test case is the lake at rest and an imposed water height on the left side wall, see Fig. 12(a). Wave gauges data [6]indicate the experimental results up to time $t = 100$ s. However, the information concerning the input wave profile (see Fig. 12(a)) at $x = 0$ is available only up to time $t = 22$ s. For numerical purpose, we suppose for $t > 22$ s, a constant free surface level $\eta = 0$ m. In practice, the first artificial reflecting waves on the wave-maker are produced around $t = 24$ s and reached the free surface gauges around $t = 30$ s. Finally, the comparisons between the experimental gauges and the numerical results will be done over a physical time of 30 secondes avoiding any wrong comparisons.

For numerical purpose, we have considered 240 initial blocks composed of 8 000 cells for the initialisation of the adaptive computation and almost 62 000 cells for uniform mesh computation. For both simulations, the CFL number is set to 0.5. Reflecting boundary conditions are prescribed to walls. Table 3 summarizes the numerical parameters used for this test case.

	Adaptive mesh simulation	Uniform mesh simulation
Simulation time	30 s	30 s
Number of blocks	240	240
Number of cells	8 000-40 000	62 000
Remeshing time step	0.25 s	not applicable
Time order integration	2	2
Space order integration	1	1
CFL	0.5	0.5
Boundary conditions	reflectives	reflectives

Table 3 Numerical parameters

In Fig. 13, to illustrate this test case we show the propagation of the wave at time $t = 11.25$ s (Fig. 13(a)), $t = 13.25$ s (Fig. 13(b)), $t = 16$ s (Fig. 13(c)) and $t = 17.5$ s (Fig. 13(d)). The free surface is colored with the kinetic energy. We also display in Fig. 14 the evolution of the mesh refinement criterion. We observe mainly that the wave front and subsequent waves are very well-captured and the mesh refinement threshold is well chosen to refine in those areas (see for instance Fig. 13(d) and 14(d)).

4.3.3 Numerical vs experimental results.

We now analyse quantitatively the numerical solution computed on adaptive and uniform mesh that we confront to the experimental measures. The obtained com-

[6] Wave gauges data are available at the address `http://nctr.pmel.noaa.gov/benchmark/Laboratory/Laboratory_MonaiValley/`

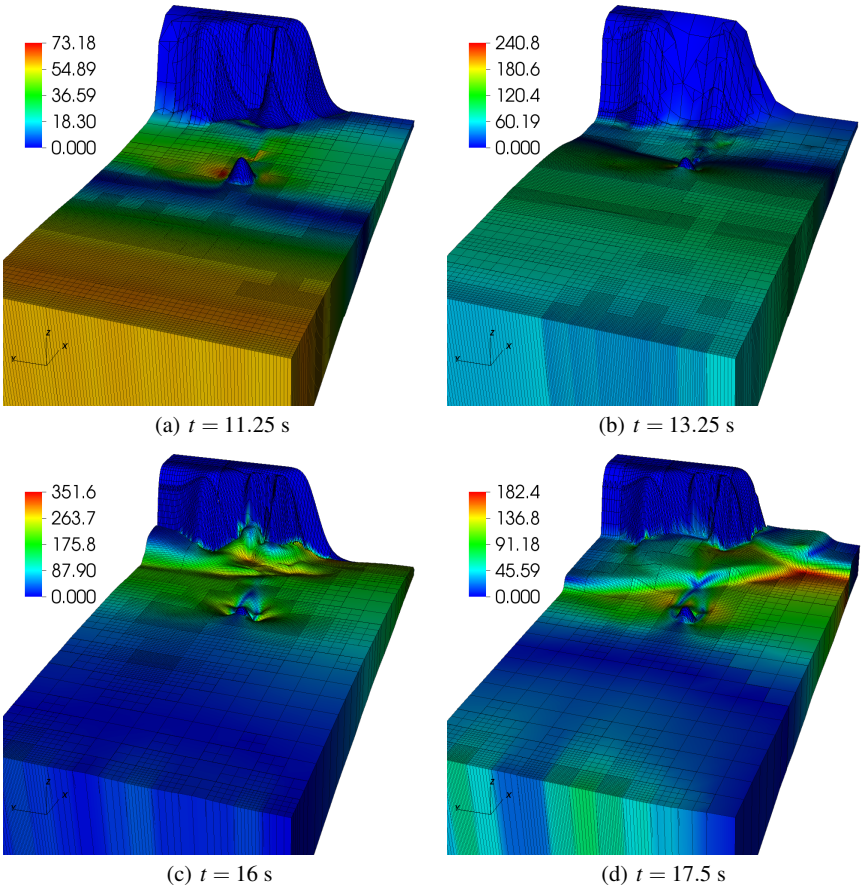

(a) $t = 11.25$ s (b) $t = 13.25$ s

(c) $t = 16$ s (d) $t = 17.5$ s

Fig. 13 Numerical water height (coloration is issue from the kinetic energy)

parisons are shown in Figs. 15 at the three waves gauges WG 1 (see Fig. 15(a)), 2 (see Fig. 15(b)) and 3 (see Fig. 15(c)). As already said before and in contrast with the two previous test cases, since the dispersive effects can be negligible, the obtained results are in a very good agreement with the experimental data.

4.3.4 Numerical results: adaptive vs uniform grid computation.

Compared to the computation on a uniform grid (Fig. 15), the adaptive mesh refinement scheme requires an average of almost 25000 cells against 62000 cells. For the same accuracy, the adaptive meshing method allows to save almost 60% of cells of the uniform simulation.

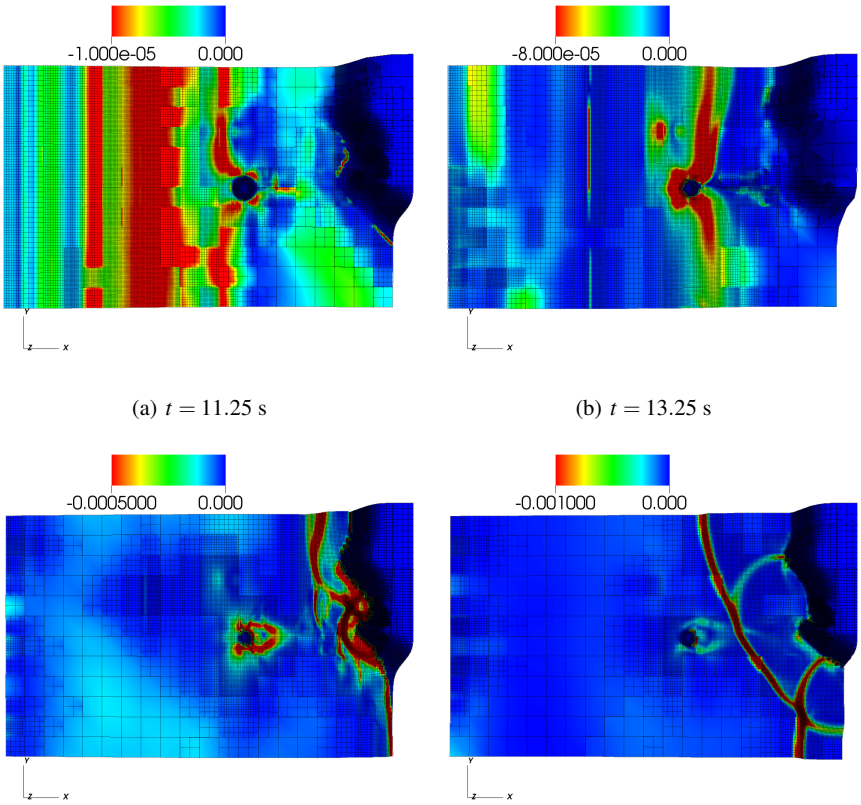

(a) $t = 11.25$ s (b) $t = 13.25$ s

(c) $t = 16$ s (d) $t = 17.5$ s

Fig. 14 Adaptive mesh (coloration is issue from the numerical density of entropy production without absolute value)

Between 3 and 7 seconds, the tsunami propagates in the domain involving a grow-up of the number of cells. Then the wave passes through the island and reaches the reef around 15 seconds. After this, the wave is reflected and goes back to the wave maker with a second interaction with the island. The maximum number of cells is reached when the wave is passing on the island and begins to run-up the coast (Figs. 13(b) and 14(b)), and when the wave goes back to the wave maker. This result is coherent with the physical process since it correspond to the two maximal flow region mixing non negligible multiple flows (smooth and discontinuous). As a consequence, reliable mesh refinement, as performed here, allows to speed up the computation by 3 times. The time evolution of the the threshold parameter and the number of cells are represented in Fig. 16(a) and Fig. 16(b).

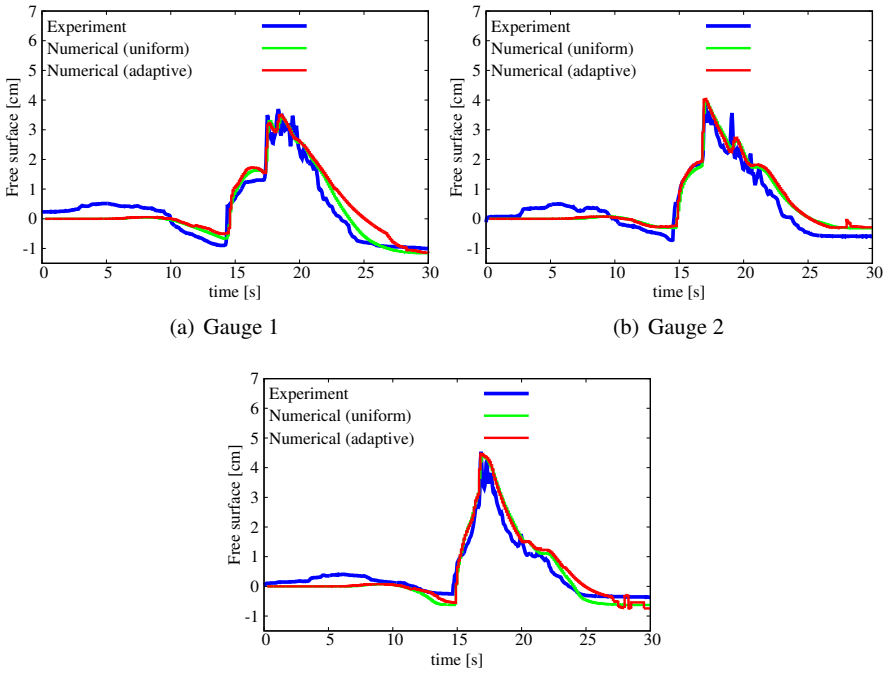

(a) Gauge 1 (b) Gauge 2

(c) Gauge 3

Fig. 15 Free surface results at different positions : experimental data versus numerical simulation with and without mesh adaptivity

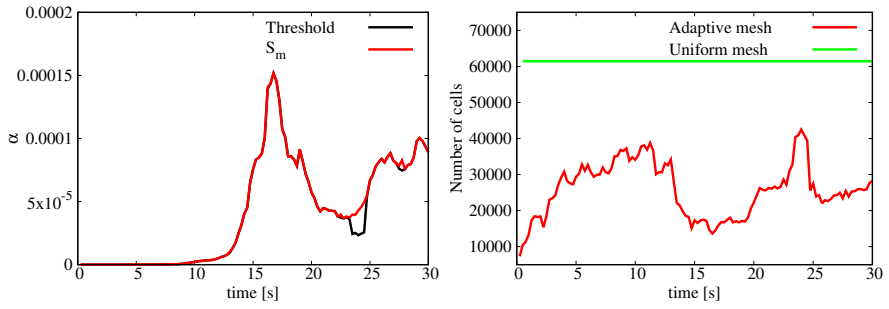

(a) Threshold (b) Number of cells

Fig. 16 Time evolution of the mesh refinement threshold and the number of cells

5 Conclusion

In the first part of this paper [41], we have introduced an analytical distribution function which allows to select automatically the mesh refinement threshold according to the local and the global maxima of the mesh refinement criterion. We have numerically investigated the efficiency of the proposed method in the case of the one dimensional Saint-Venant system. As a natural extension, we have proposed here, the numerical validation of our approach for the one and two-dimensional non homogeneous Saint-Venant system confronted to several experimental test cases. For each test case, we have shown that the adaptive scheme allows to save computational time keeping the same order of accuracy when compared to the numerical solution computed on a uniform. In particular, it shows that the method to select automatically the threshold parameter, based on the distribution function, is efficient. Moreover, for each test case, we have pointed out that following the type of flows, the threshold is well-chosen to define the region of the domain to be refined. Finally, in contrast with existing methods in the literature, this method does not require any tunable coefficient and can be applied for any test cases.

Acknowledgments

This work is partially supported the Project MTM2011-29306-C01-01 from the MICINN (Spain) and the French national research project TANDEM (Tsunamis in the Atlantic and the English channel : definition of the effects through numerical modeling), the French government (Projets Investissement d'Avenir, agreement reference number ANR-11-RSNR-0023-01).

References

1. Altazin, T., Ersoy, M., Golay, F., Sous, D., Yuschenki, L.: Numerical investigation of bb-amr scheme using entropy production as refinement criterion. Accepted in International Journal of Computational Fluid Dynamics (2016)
2. Altmann, C., Belat, T., Gutnic, M., Helluy, P., Mathis, H., Sonnendrücker, E., Angulo, W., Hérard, J.: A local time-stepping discontinuous Galerkin algorithm for the MHD system. In: CEMRACS 2008—Modelling and numerical simulation of complex fluids, *ESAIM Proc.*, vol. 28, pp. 33–54. EDP Sci., Les Ulis (2009). DOI 10.1051/proc/2009038. URL http://dx.doi.org/10.1051/proc/2009038
3. Audusse, E., Bouchut, F., Bristeau, M.O., Klein, R., Perthame, B.: A fast and stable well-balanced scheme with hydrostatic reconstruction for shallow water flows. SIAM Journal on Scientific Computing **25**(6), 2050–2065 (2004)
4. Berger, M., Colella, P.: Local adaptive mesh refinement for shock hydrodynamics. Journal of Computational Physics **82**(1), 64 – 84 (1989). DOI http://dx.doi.org/10.1016/0021-9991(89)90035-1. URL http://www.sciencedirect.com/science/article/pii/0021999189900351

5. Berger, M., Oliger, J.: Adaptive mesh refinement for hyperbolic partial differential equations. J. Comp. Phys. **53**(3), 484–512 (1984)
6. Bonneton, P.: Analyse physique et modélisation des processus hydrodynamiques en zone de surf. Oceanis pp. 157–179 (2003)
7. Bourdarias, C., Ersoy, M., Gerbi, S.: A model for unsteady mixed flows in non uniform closed water pipes and a well-balanced finite volume scheme. Int. J. Finite Vol. **6**(2), 47 (2009)
8. Bourdarias, C., Ersoy, M., Gerbi, S.: A kinetic scheme for transient mixed flows in non uniform closed pipes: a global manner to upwind all the source terms. J. Sci. Comput. **48**(1-3), 89–104 (2011). DOI 10.1007/s10915-010-9456-0. URL http://dx.doi.org/10.1007/s10915-010-9456-0
9. Bourdarias, C., Ersoy, M., Gerbi, S.: A mathematical model for unsteady mixed flows in closed water pipes. Sci. China Math. **55**(2), 221–244 (2012). DOI 10.1007/s11425-011-4353-z. URL http://dx.doi.org/10.1007/s11425-011-4353-z
10. Bourdarias, C., Ersoy, M., Gerbi, S.: Air entrainment in transient flows in closed water pipes: a two-layer approach. ESAIM: M2AN **47**(2), 507–538 (2013). DOI 10.1051/m2an/2012036. URL http://dx.doi.org/10.1051/m2an/2012036
11. Coupez, T., Hachem, E.: Solution of high-reynolds incompressible flow with stabilized finite element and adaptive anisotropic meshing. Computer Methods in Applied Mechanics and Engineering **267**(0), 65 – 85 (2013). DOI http://dx.doi.org/10.1016/j.cma.2013.08.004. URL http://www.sciencedirect.com/science/article/pii/S0045782513002077
12. Dutykh, D., Acary-Robert, C., Bresch, D.: Mathematical modeling of powder-snow avalanche flows. Studies in Applied Mathematics **127**(1), 38–66 (2011)
13. Dutykh, D., Dias, F.: Energy of tsunami waves generated by bottom motion. Proceedings of the Royal Society of London A: Mathematical, Physical and Engineering Sciences **465**(2103), 725–744 (2009)
14. Ersoy, M.: Modélisation, analyse mathématique et numérique de divers écoulements compressibles ou incompressibles en couche mince. Ph.D. thesis, Université de Savoie (2010). Available at http://tel.archives-ouvertes.fr/tel-00529392
15. Ersoy, M.: Dimension reduction for incompressible pipe and open channel flow including friction. In: J. Brandts, S. Korotov, M. Krizek, K. Segeth, J. Sistek, T. Vejchodsky (eds.) Conference Applications of Mathematics 2015, in honor of the birthday anniversaries of Ivo Babuska (90), Milan Prager (85), and Emil Vitasek (85). Institute of Mathematics CAS (2015)
16. Ersoy, M.: Dimension reduction for compressible pipe flows including friction. Accepted in Asymptotic Analysis **-**(-), – (2016)
17. Ersoy, M., Golay, F., Yushchenko, L.: Adaptive multiscale scheme based on numerical density of entropy production for conservation laws. Cent. Eur. J. Math. **11**(8), 1392–1415 (2013). DOI 10.2478/s11533-013-0252-6. URL http://dx.doi.org/10.2478/s11533-013-0252-6
18. Ersoy, M., Lakkis, O., Townsend, P.: An energetically consistent saint-venant system for overland flows. submitted **-**, – (2016)
19. Ersoy, M., Ngom, T.: Existence of a global weak solution to compressible primitive equations. C. R. Math. Acad. Sci. Paris **350**(7-8), 379–382 (2012). DOI 10.1016/j.crma.2012.04.013. URL http://dx.doi.org/10.1016/j.crma.2012.04.013
20. Ersoy, M., Ngom, T., Sy, M.: Compressible primitive equations: formal derivation and stability of weak solutions. Nonlinearity **24**(1), 79–96 (2011). DOI 10.1088/0951-7715/24/1/004. URL http://dx.doi.org/10.1088/0951-7715/24/1/004
21. Eymard, R., T., G., Herbin, R.: Finite volume methods. In: Handbook of numerical analysis, Vol. VII, Handb. Numer. Anal., VII, pp. 713–1020. North-Holland, Amsterdam (2000)
22. Faccanoni, G., Mangeney, A.: Exact solution for granular flows. International Journal for Numerical and Analytical Methods in Geomechanics (2012). DOI 10.1002/nag.2124. URL https://hal.inria.fr/hal-00776614
23. Fernández-Nieto, E.D., Bouchut, F., Bresch, D., Diaz, M.C., Mangeney, A.: A new savage–hutter type model for submarine avalanches and generated tsunami. Journal of Computational Physics **227**(16), 7720–7754 (2008)

24. Fuster, D., Agbaglah, G., Josserand, C., Popinet, S., Zaleski, S.: Numerical simulation of droplets, bubbles and waves: state of the art. Fluid Dynamics Research **41**(6), 065,001 (2009)
25. Gerbeau, J.F., Perthame, B.: Derivation of viscous Saint-Venant system for laminar shallow water; numerical validation. Discrete Cont. Dyn. Syst. Ser. B **1**(1), 89–102 (2001)
26. Godlewski, E., Raviart, P.: Numerical approximation of hyperbolic systems of conservation laws, *Applied Mathematical Sciences*, vol. 118. Springer-Verlag, New York (1996)
27. Golay, F.: Numerical entropy production and error indicator for compressible flows. Comptes Rendus Mécanique **337**(4), 233–237 (2009)
28. Golay, F., Ersoy, M., Yushchenko, L., Sous, D.: Block-based adaptive mesh refinement scheme using numerical density of entropy production for three-dimensional two-fluid flows. International Journal of Computational Fluid Dynamics **29**(1), 67–81 (2015)
29. Hachem, E., Feghali, S., Codina, R., Coupez, T.: Immersed stress method for fluid structure interaction using anisotropic mesh adaptation. International Journal for Numerical Methods in Engineering **94**(9), 805–825 (2013). DOI 10.1002/nme.4481. URL `http://dx.doi.org/10.1002/nme.4481`
30. Houston, P., Mackenzie, J., Süli, E., Warnecke, G.: A posteriori error analysis for numerical approximations of Friedrichs systems. Numer. Math. **82**(3), 433–470 (1999)
31. Karni, S., Kurganov, A.: Local error analysis for approximate solutions of hyperbolic conservation laws. Adv. Comput. Math. **22**(1), 79–99 (2005)
32. Karni, S., Kurganov, A., Petrova, G.: A smoothness indicator for adaptive algorithms for hyperbolic systems. J. Comp. Phys. **178**(2), 323–341 (2002)
33. Kervella, Y., Dutykh, D., Dias, F.: Comparison between three-dimensional linear and nonlinear tsunami generation models. Theoretical and computational fluid dynamics **21**(4), 245–269 (2007)
34. Liu, P.L., Synolakis, C.: Advanced numerical models for simulating tsunami waves and runup, *Advances in Coastal and Ocean Engineering*, vol. 10, liu, philip lf and synolakis, costas edn. School of Civil and Environmental Engineering (2008)
35. Losasso, F., Gibou, F., Fedkiw, R.: Simulating water and smoke with an octree data structure. ACM Trans. Graph. **23**(3), 457–462 (2004). DOI 10.1145/1015706.1015745. URL `http://doi.acm.org/10.1145/1015706.1015745`
36. Lynett, P.J., Swigler, D., Son, S., Bryant, D., Socolofsky, S.: Experimental study of solitary wave evolution over a 3d shallow shelf. Coastal Engineering Proceedings **1**(32), 1 (2011)
37. Mangeney, A., Bouchut, F., Thomas, N., Vilotte, J.P., Bristeau, M.O.: Numerical modeling of self-channeling granular flows and of their level-channel deposits. J. of Geophys. Res. **112**, 1–21 (2007)
38. Marche, F.: Derivation of a new two-dimensional viscous shallow water model with varying topography, bottom friction and capillary effects. European Journal of Mechanic. B, Fluids **26**(1), 49–63 (2007)
39. Min, C., Gibou, F.: A second order accurate level set method on non-graded adaptive cartesian grids. Journal of Computational Physics **225**(1), 300 – 321 (2007). DOI http://dx.doi.org/10.1016/j.jcp.2006.11.034. URL `http://www.sciencedirect.com/science/article/pii/S0021999106005912`
40. Mungkasi, S., Roberts, S.G.: Numerical entropy production for shallow water flows. In: W. McLean, A.J. Roberts (eds.) Proceedings of the 15th Biennial Computational Techniques and Applications Conference, CTAC-2010, *ANZIAM J.*, vol. 52, pp. C1–C17 (2011). `http://anziamj.austms.org.au/ojs/index.php/ANZIAMJ/article/view/3786` [April 9, 2011]
41. Pons, K., Ersoy, M.: Adaptive mesh refinement method. Part 1: Automatic thresholding based on a distribution function. (2016)
42. Popinet, S.: Adaptive modelling of long-distance wave propagation and fine-scale flooding during the tohoku tsunami. Nat. Hazards Earth Syst. Sci **12**(4), 1213–1227 (2012)
43. Roeber, V., Cheung, K.F.: Boussinesq-type model for energetic breaking waves in fringing reef environments. Coastal Engineering **70**, 1–20 (2012)
44. Roeber, V., Cheung, K.F., Kobayashi, M.H.: Shock-capturing boussinesq-type model for nearshore wave processes. Coastal Engineering **57**(4), 407–423 (2010)

45. Toro, E.F.: Riemann solvers and numerical methods for fluid dynamics, third edn. Springer-Verlag, Berlin (2009). DOI 10.1007/b79761. URL http://dx.doi.org/10.1007/b79761
46. Williamschen, M.J., Groth, C.: Parallel anisotropic block-based adaptive mesh refinement algorithm for three-dimensional flows. In: 21st AIAA Computational Fluid Dynamics Conference, June 24-27, San Diego, CA, pp. 1–22 (2013)
47. Yiu, K., Greaves, D., Cruz, S., Saalehi, A., Borthwick, A.: Quadtree grid generation: Information handling, boundary fitting and cfd applications. Computers & Fluids **25**(8), 759 – 769 (1996). DOI http://dx.doi.org/10.1016/S0045-7930(96)00029-1. URL http://www.sciencedirect.com/science/article/pii/S0045793096000291
48. Zhang, M., Wu, W.: A two dimensional hydrodynamic and sediment transport model for dam break based on finite volume method with quadtree grid. Applied Ocean Research **33**(4), 297 – 308 (2011). DOI http://dx.doi.org/10.1016/j.apor.2011.07.004. URL http://www.sciencedirect.com/science/article/pii/S0141118711000563
49. Zheng, Z., Groth, C.: Block-based adaptive mesh refinement finite-volume scheme for hybrid multi-block meshes. In: 7st conference on Computational Fluid Dynamics (ICCFD7), July 9-13, Hawaii, pp. 1–19 (2012)